



Cite this: *RSC Adv.*, 2017, 7, 48238

Morphology control and enhancement of 1.5 μm emission in $\text{Ca}^{2+}/\text{Ce}^{3+}$ codoped $\text{NaGdF}_4:\text{Yb}^{3+}, \text{Er}^{3+}$ submicrorods

Jiangyun Dai,^a Chao Yang,^a Hong Zhang,^a Hua Zhang,^a Guoying Feng^{*a} and Shouhuan Zhou^{*ab}

The successful synthesis of rare earth doped nano/microcrystals with the desired morphology, uniform monodispersity, and intense infrared emission is of fundamental significance, and would facilitate their application in infrared emission-related miniaturization and integration in optoelectronics. However, simultaneously controlling the morphology and enhancing the infrared emission through simple and effective methods has not been well explored. In this study, *via* Ca^{2+} doping with an optimized concentration of 25 mol% in the hydrothermal solution, irregular $\text{NaGdF}_4:\text{Yb}/\text{Er}$ submicrocrystals converted into highly uniform submicrorods. Meanwhile, an obvious enhancement of visible upconversion (UC) and near-infrared (NIR) downconversion (DC) emission were obtained, probably due to the improved morphology and lowering the local crystal field symmetry around the rare earth ions induced by Ca^{2+} doping. Furthermore, Ce^{3+} ions with an optimized concentration of 2 mol% were codoped to intentionally tailor the branching ratio through efficient energy transfer from Er^{3+} to Ce^{3+} . As a result, the ~ 1530 nm emission intensity of the $\text{NaGdF}_4: 25\text{Ca}/2\text{Ce}/20\text{Yb}/2\text{Er}$ submicrorods increased by about 6.4 times in comparison with the $\text{NaGdF}_4:20\text{Yb}/2\text{Er}$ counterpart.

Received 26th July 2017
Accepted 9th October 2017

DOI: 10.1039/c7ra08254a

rsc.li/rsc-advances

1. Introduction

In the past decades, rare earth doped materials, which are able to exhibit infrared DC emission in addition to their visible UC emission of lanthanide ions, have attracted considerable attention due to their favorable merits, such as large anti-Stokes shifts, long excited-state lifetimes, narrow emission bandwidths and high photostability.^{1–4} Based on these inherent advantages, rare earth doped materials play an important role in fabricating the active optical components in optoelectronic applications like laser materials, flat-panel displays, and optical sensors.^{5–9} Notably, rare earth doped nano/microcrystals are of great importance for expanding the applications of miniaturized and integrated optoelectronics.^{10,11} Among the rare earth ions, Er^{3+} is especially attractive because of its NIR emission wavelength of approximately 1530 nm, which lies in the low-loss telecommunication window in optical communication.^{12,13} However, the low intra-4f-configurational absorption cross section of Er^{3+} commonly leads to a weak emission intensity upon inefficient pumping.¹⁴ Fortunately, Yb^{3+} ions possess a higher absorption cross section and its $^2\text{F}_{5/2}$ energy level is resonant with the $^4\text{I}_{11/2}$

energy level of Er^{3+} . Thus, introduction of Yb^{3+} as an ideal sensitizer can realize efficient NIR emission of Er^{3+} upon excitation at 980 nm.

It is well established that the optical, electrical and magnetic properties of nano/microcrystals are depended on not only their composition, but also their geometrical factors including phase, morphology and size. Especially, when the rare earth doped materials are synthesized in the form of the one-dimensional nano/microstructures, they would stimulate great attention due to their marked shape-specific and quantum-confinement effects.^{15,16} Although several methods have been used to synthesize the one-dimensional nano/microcrystals with a well defined morphology, finding a novel and facile strategy is still imperative.¹⁵ Furthermore, to realize their practical applications, simultaneously obtaining an efficient infrared optical signal is also desired. Hence, many efforts have been devoted to optimizing the performance of rare earth doped materials by adopting novel strategies, such as dye sensitizing,¹⁷ core-shell structure,^{18,19} and host lattice manipulation.²⁰ Impressively, host lattice manipulation *via* impurity doping, which has the ability to modify the electron charge density and crystal symmetry of rare earth ions, could simultaneously enhance the emission intensity and control the well-defined morphology in a facile and straightforward way.^{21,22} Although many previous works have adopted this strategy to enhance the visible or NIR UC emission,^{23–25} enhancing the luminescence in the NIR DC emission range has rarely been studied.

^aInstitute of Laser and Micro/Nano Engineering, College of Electronics and Information Engineering, Sichuan University, Chengdu 610064, China. E-mail: guoying_feng@scu.edu.cn

^bNorth China Research Institute of Electro-Optics, Beijing 100015, China. E-mail: zhoush@scu.edu.cn



For Er³⁺ doped materials, NIR emission at 1530 nm is always accompanied by the visible UC emission upon excitation at 980 nm. However, the visible emission is undesired in the field of infrared application (*e.g.*, optical amplifiers), which would reduce the intensity of NIR emission (~1530 nm) of Er³⁺ ions. One of the approaches to circumvent these obstacles is to improve the low branching ratio for the NIR emission. Recent reports show doping with Ce³⁺ ions can significantly enhance the ⁴I_{11/2} → ⁴I_{13/2} transition probability of Er³⁺.^{26,27} The possible mechanism is the non-radiative phonon-assisted energy transfer ²F_{5/2}(Ce³⁺) + ⁴I_{11/2}(Er³⁺) → ²F_{7/2}(Ce³⁺) + ⁴I_{13/2}(Er³⁺) which facilitates the population of ⁴I_{13/2} of Er³⁺ and decreases UC emission. Therefore, based on the forementioned theories, codoping Ca²⁺ and Ce³⁺ in the crystals would synergistically enhance NIR emission.

In this work, *via* doping impurity Ca²⁺ ions into the host lattices by substituting Gd³⁺ ions, we demonstrated the irregular NaGdF₄:Yb/Er submicrocrystals converted into well-defined submicrorods, and the visible UC and NIR DC emission were enhanced through a facile and effective hydrothermal method. Additionally, benefiting from the highly efficient energy transfer from Er³⁺ to Ce³⁺ by co-doping Ce³⁺, the NIR DC was further enhanced by about 6.4 times in comparison with that of the NaGdF₄:Yb/Er counterpart.

2. Experimental

2.1 Materials and reagents

Ethylenediamine tetraacetic acid (EDTA > 99.4%) was supplied by Sigma-Aldrich. Gd(NO₃)₃·6H₂O (99.99%), Er(NO₃)₃·5H₂O (99.9%), Yb(NO₃)₃·5H₂O (99.9%), sodium hydroxide (NaOH > 96.0%), ammonium fluoride (NH₄F > 98.0%), and highly concentrated nitric acid were purchased from Aladdin Chemical Reagent Co. All chemicals were of analytical grade and were used directly as received without further purification, deionized water was used throughout.

2.2 Synthesis of 20% Yb³⁺, 2% Er³⁺:NaGdF₄ submicrocrystals

The rare-earth doped NaGdF₄ (1 mmol) submicrocrystals were synthesized by a hydrothermal method. Firstly, 12.5 ml of aqueous solution containing 0.4 g EDTA and 1.05 ml of NaOH aqueous solution (5.0 M) were mixed under stirring until the solution becomes even. Subsequently, 5 ml of Ln(NO₃)₃ (Ln = Gd, Yb, Er) aqueous solutions (0.2 M), 8 ml of NH₄F (2.0 M) aqueous solutions and 7 ml dilute nitric acid (1 M) were added to the mixture. After agitating at room temperature for 90 min, the resultant solution was poured into a 50 ml Teflon-lined autoclave and heated subsequently to 190 °C for 48 h. Finally, the autoclave was cooled to room temperature naturally. The products deposited at the bottom of the vessel were collected by centrifugation, washed with deionized water and ethanol several times, and then dried at 60 °C for 24 h in air. The procedure for the synthesis of the Ca²⁺ doped, Ce³⁺ doped and Ca²⁺/Ce³⁺ codoped 20% Yb³⁺, 2% Er³⁺:NaGdF₄ submicrocrystals were similar to the case of the 20% Yb³⁺, 2% Er³⁺:NaGdF₄ submicrocrystals.

2.3 Characterization

The X-ray powder diffraction (XRD) patterns were carried out with a powder diffractometer (Japan Rigaku D/max-rB) with Cu Kα radiation (λ = 0.154 178 nm). The morphology was studied using a field-emission scanning electron microscope (FESEM) operated at an acceleration voltage of 5 kV (HitachiSU-8220). The NIR luminescence spectroscopy was recorded by a monochromator (Princeton Instrument SP2750) equipped with an InGaAs infrared detector (ACTON), the UC luminescence spectroscopy were measured by a single mode fiber with an Ocean Optics USB4000 spectrometer (optical resolution ~0.2 nm) using a continuous 980 nm laser from a semiconductor laser as the excitation source, and the area of the samples that were exposed to the laser radiation was about 1.5 mm². The decay time was measured by a digital phosphor oscilloscope (Tektronix DPO 4032) using the 980 nm laser from an OPO (an optical parametric oscillation, INNOLAS) as the excitation source. All the measurements were implemented at room temperature (RT).

3. Results and discussion

3.1 Morphology and crystal structure

It should be pointed out that rare earth doped fluorides with high quality and anisotropic morphology could be synthesized in an appropriately surplus F⁻/Ln³⁺ molar ratio.^{28–31} In this view, the F⁻/Ln³⁺ molar ratio was set to be 16. A series of 20% Yb/2% Er:NaGdF₄ crystals doped with different Ca²⁺ and Ce³⁺ concentration were synthesized and the corresponding XRD patterns are shown in Fig. 1. XRD patterns (Fig. 1a) suggest that the samples of different Ca²⁺ doping concentration are identical with JCPDS Card (no. 27-0699), showing that the Ca²⁺ are completely embedded into the crystal lattice of NaGdF₄ by replacing the sites of Gd³⁺ ions, without finding obvious shifting of diffraction peaks due to the F⁻ vacancies and ionic radius difference between Gd³⁺ and Ca²⁺.²⁴ Fig. 1b shows the X-ray diffraction patterns of 20% Yb/2% Er:NaGdF₄ crystals doped with different Ce³⁺ concentration. No additional peaks are observed, indicating that the doping Ce³⁺ ions have a negligible effect on the phase structure and Ce³⁺ ions have substituted the Gd³⁺ sites in the NaGdF₄ host. Notably, the X-ray diffraction patterns of 20% Yb/2% Er:NaGdF₄ crystals codoped with 25% Ca²⁺ and 2% Ce³⁺ are also given in Fig. 1b, which can be still indexed to the β-NaGdF₄ phase. The schematic diagram of β-NaGdF₄ crystal structure and coordination environment of Na⁺/Gd³⁺ ions are shown in Fig. 1c. There are three types of cationic sites in the unit cell of β-NaGdF₄: a six-fold coordinated one occupied by Na⁺ and vacancies, a nine-fold coordinated position occupied by Gd³⁺, and another nine-fold coordinated site occupied randomly by Na⁺ and Gd³⁺. The two different Gd³⁺ sites are coordinated in the form of tricapped trigonal prisms.³²

FESEM were then carried out to study the morphology and size of NaGdF₄:20% Yb/2% Er samples doped with different Ca²⁺ and Ce³⁺ doping concentrations. Fig. 2a presents the FESEM image of the NaGdF₄:20% Yb/2% Er submicrocrystals without Ca²⁺ doping and shows irregular microrods. Notably,



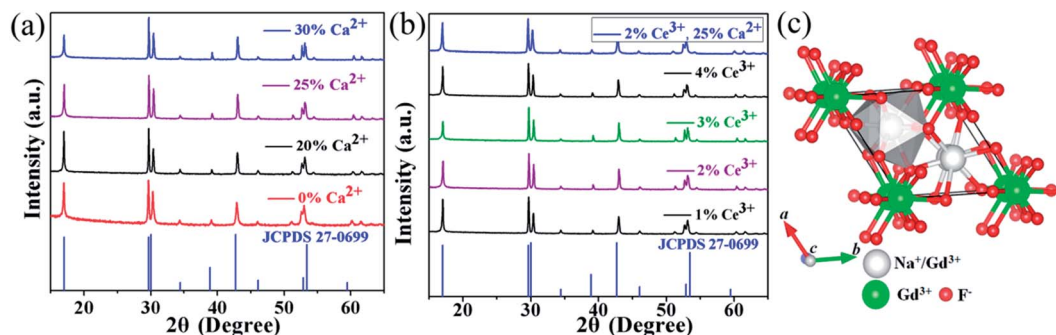


Fig. 1 XRD patterns of the NaGdF₄:xCa/yCe/20Yb/2Er samples, (a) $x = 0\%$, 20% , 25% , 30% , $y = 0$; (b) $x = 0$, $y = 1\%$, 2% , 3% , 4% . (c) Schematic illustration of β -NaGdF₄ structure and coordination environment of the Na⁺/Gd³⁺.

many cracks are observed on the surface, which could be ascribed to the microrods deriving from decreasing the core of spherical aggregates and extruding between the growing microrods.³³ Interestingly, once doped 20% Ca²⁺ in the NaGdF₄: 20% Yb/ 2% Er sample, the crystals (Fig. 2b) exhibit uniform hexagonal submicrorods, although with a wide size distribution. Further increasing the doping content of Ca²⁺ results in a more even size distribution. Furthermore, when the crystal size is denoted as “length \times radius”, the mean size of NaGdF₄:xCa/20Yb/2Er ($x = 0\%$, 20% , 25% , 30%) crystals are measured to be 0.38×0.96 , 0.24×1.26 , 0.21×1.34 and 0.33×1.82 μm , respectively. Without the help of Ca²⁺ doping, the morphology of NaGdF₄:xCe/20Yb/2Er ($x = 1\%$, 2% , 3% , 4%)

crystals still inherit irregular submicrorods as that of NaGdF₄: 20% Yb/2Er, the typical FESEM image of NaGdF₄: 2% Ce/20Yb/2Er crystal is shown in Fig. 2e. With codoping of 25% Ca²⁺ and 2% Ce³⁺, the sample keep highly uniform submicrorods (Fig. 2f).

Based on the results stated above, the effect induced by Ca²⁺ doping on the morphology evolution of NaGdF₄ submicrocrystals is proposed, as schematically shown in Fig. 3. First of all, it is essential to have a full understanding of the crystal growth of NaGdF₄ submicrocrystals without Ca²⁺ doping. As is well known, hexagonal NaGdF₄ has a very close crystalline structure with hexagonal NaYF₄, so they may undergo a same crystal growth kinetic process in the similar hydrothermal condition.³¹ The irregular NaGdF₄ submicrorods with cracked surface were obtained due to two main factors. One is that final submicrorods originate from decreasing the core of spherical aggregates and extruding between the growing submicrorods.³³ And another one is that the fast growth rate of the top/bottom planes would hinder the continuing growth of six energetically equivalent prismatic side planes.^{29,34} Once upon doping Ca²⁺ in the reaction solution, extra F⁻ ions are remaining in system due to charge compensation and a transient electric dipole with the positive pole pointing outward is also formed on the grain surface.^{24,35,36} Both of them accelerate the diffusion of F⁻ ions in the system under the control of monomer diffusion to the grain surface by attractive interaction,^{36,37} finally facilitating the anisotropic growth of NaGdF₄ submicrorods. Hence,

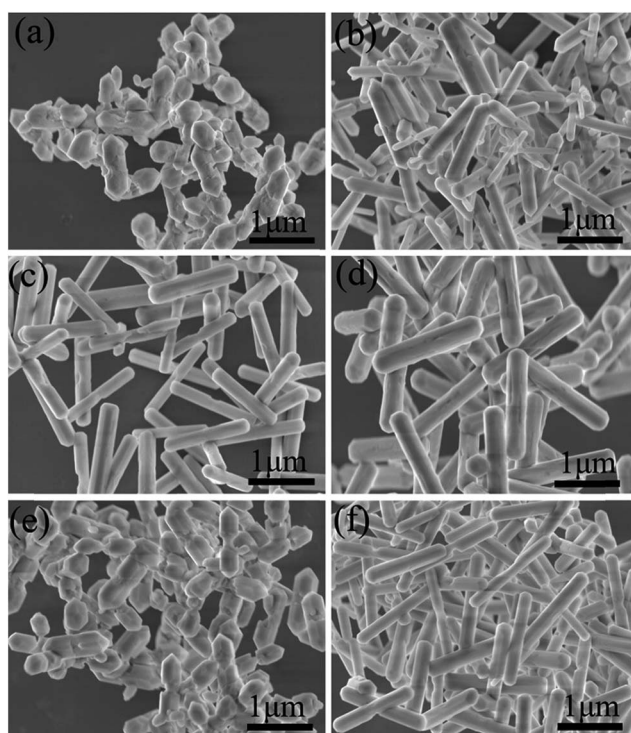


Fig. 2 FESEM images of NaGdF₄: 20% Yb/ 2% Er submicrocrystals doped with (a) 0% Ca²⁺, (b) 20% Ca²⁺, (c) 25% Ca²⁺, (d) 30% Ca²⁺, (e) 2% Ce³⁺, (f) 2% Ce³⁺, 25% Ca²⁺.

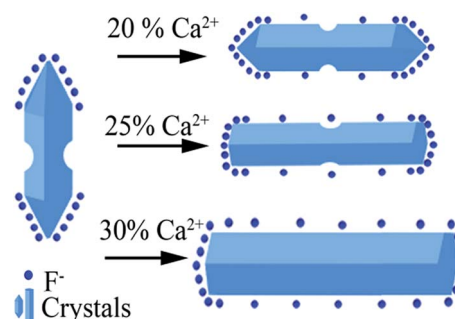


Fig. 3 Schematic illustration of possible mechanism of Ca²⁺ doping and its effect on morphology evolution of NaGdF₄ submicrocrystals.



along with increasing Ca^{2+} doping content, the surface is becoming more smooth and the size distribution more even. It should be noting that the sharp ends of NaGdF_4 crystals tend to be more flat ends, which is indirect evidence of F^- concentration increasing only induced by Ca^{2+} doping.³⁸

3.2 Optical properties

Fig. 4a shows the visible UC emission spectra of the $\text{NaGdF}_4:20\% \text{Yb}/2\% \text{Er}$ submicrocrystals doped with different Ca^{2+} concentrations, which are recorded under 980 nm laser excitation with the pump power of 150 mW. It is observed that there are three UC bands, centred at 519, 537, and 652 nm, which are ascribed to $^2\text{H}_{11/2} \rightarrow ^4\text{I}_{15/2}$ (519 nm), $^4\text{S}_{3/2} \rightarrow ^4\text{I}_{15/2}$ (537 nm), $^4\text{F}_{9/2} \rightarrow ^4\text{I}_{15/2}$ (652 nm), respectively. Meanwhile, an obvious enhancement of the UC emission is observed upon 20% Ca^{2+} doping. The enhancement reaches the most at 25% Ca^{2+} doping, then declining with further increasing the Ca^{2+} concentration to 30%. Furthermore, the integrated visible UC emission intensity of crystals doped with 25% Ca^{2+} is about 5.1 times higher than that of the crystals without Ca^{2+} doping. To investigate the effect of Ca^{2+} doping on the UC emission, we first determined the number of photons required for the red and green luminescence intensity, which obey the following relationship with the pumping power:³⁹

$$I_{\text{up}} = P^n \quad (1)$$

where I_{up} is the UC emission intensity, P is the infrared pumping power, and n is the number of pumping photons required for emitting one UC photon. From the logarithmic plots of the UC luminescence intensity as a function of the excitation power (Fig. 4c and d), it can be concluded that both green and red emission are two-photon absorption process in the presence and absence of Ca^{2+} , indicating that Ca^{2+} doping does not alter the UC mechanism. The gradual enhancement in UC luminescence induced by Ca^{2+} doping is ascribed to two factors including lowering the local crystal field symmetry around rare earth ions and improving the morphology of the NaGdF_4 submicrocrystals. However, when Ca^{2+} doping concentration is beyond 25%, more F^- vacancies are forming, which reduce the UC emission intensity.^{24,36} Based on these results, we expect that the 1530 nm emission intensity of Er^{3+} ion could also be enhanced upon doping Ca^{2+} .

Fig. 5 shows the NIR emission spectra of the submicrocrystals, which are recorded at the pump power of 270 mW. Obviously, the characteristic emission peak centered at 1535 nm is attributed to the $^4\text{I}_{13/2} \rightarrow ^4\text{I}_{15/2}$ transitions of Er^{3+} ions. The NIR emission intensity increases with Ca^{2+} dopant concentrations from 0% to 25% before declining as Ca^{2+} dopant concentration is increased to 30% (Fig. 5a). The integrated NIR DC emission intensity shows an identical trend to that of the visible UC emission. Therefore, the optimum Ca^{2+} dopant concentration is determined to be 25%. Next, to further

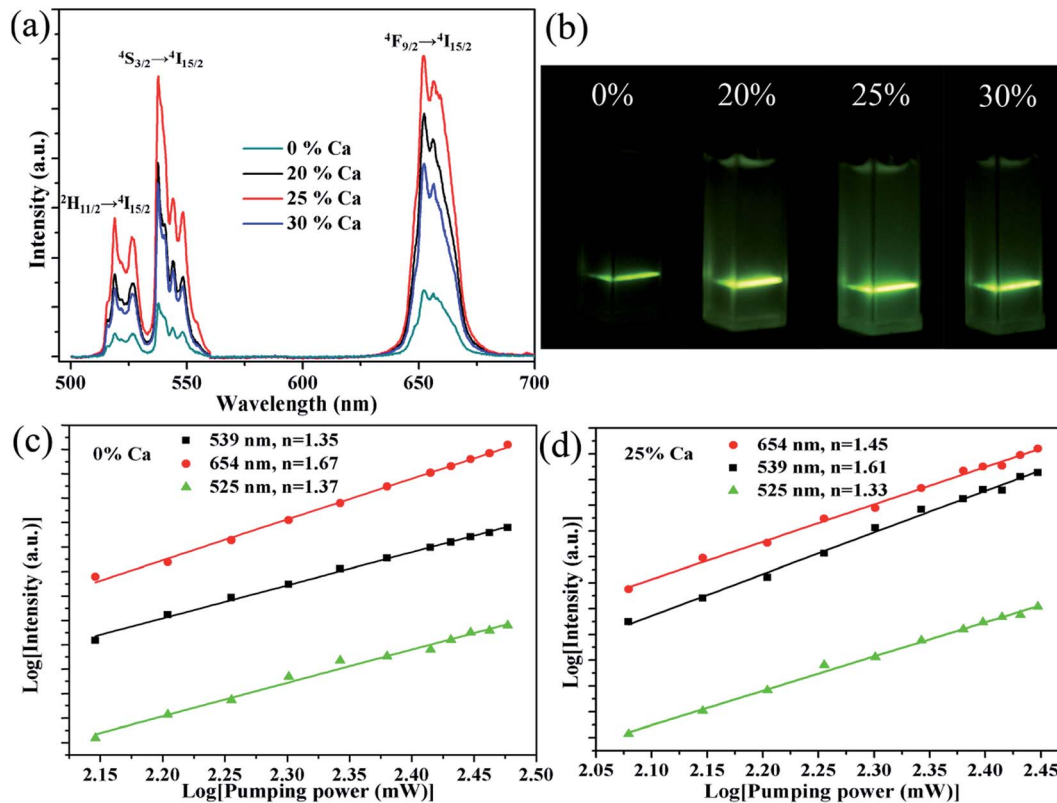


Fig. 4 UC emission spectra of $\text{NaGdF}_4:20\text{Yb}/2\text{Er}/x\text{Ca}$ ($x = 0\%, 20\%, 25\%, 30\%$) under 980 nm laser excitation. (b) The corresponding photographs of the submicrocrystals dispersed in water. log–log plots of the UC emission intensity against laser excitation power for $\text{NaGdF}_4:20\text{Yb}/2\text{Er}$ (c), and $\text{NaGdF}_4:25\text{Ca}/20\text{Yb}/2\text{Er}$ (d).



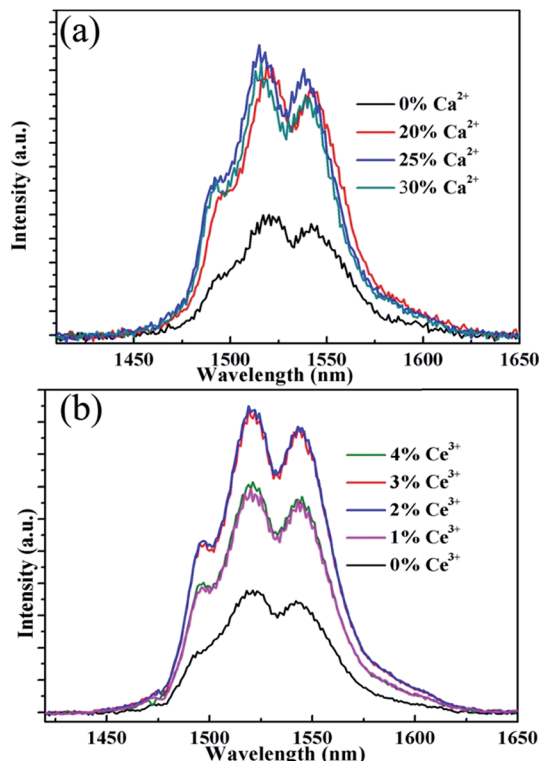


Fig. 5 NIR emission spectra of the sample $\text{NaGdF}_4:x\text{Ca}/y\text{Ce}/20\% \text{Yb}/2\% \text{Er}$. (a) $x = 0\%$, 20% , 25% , 30% , $y = 0$; (b) $x = 0$, $y = 1\%$, 2% , 3% , 4% under 980 nm laser excitation.

investigate the effect of Ce^{3+} concentration on the NIR emission properties, we systematically investigated the NIR emission spectra of $\text{NaGdF}_4:20\text{Yb}/2\text{Er}/x\text{Ce}$ ($x = 1\%$, 2% , 3% , 4%) crystals obtained upon excitation at 980 nm and the results are summarized in Fig. 5b. As the concentration of Ce^{3+} ions increases from 0 to 2%, the NIR emission significantly increases and reaches the most. The enhanced NIR emission arises from the efficient non-radiative phonon-assisted energy transfer between the $^4\text{I}_{11/2} \rightarrow ^4\text{I}_{13/2}$ transition of Er^{3+} ions and the $^2\text{F}_{5/2} \rightarrow ^2\text{F}_{7/2}$ transition of Ce^{3+} ions, which improves the branching ratio of NIR emission and suppress the visible emission by

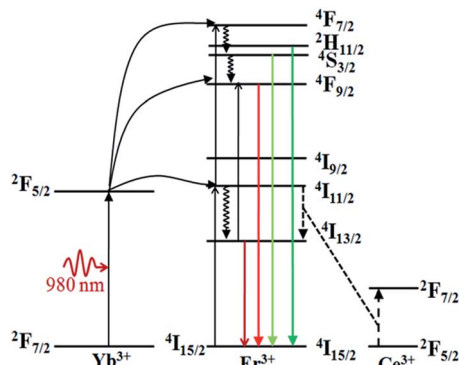


Fig. 6 Energy level diagram of Yb^{3+} ion, Er^{3+} ion, Ce^{3+} ion, as well as the relevant transitions under the 980 nm laser excitation.

altered the UC pathways.^{26,27} All these transitions are illustrated in an energy levels diagram in Fig. 6.

It is essential to compare the NIR emission intensity of samples doped with the optimum Ca^{2+} and Ce^{3+} dopant concentration. Through measuring the integrated NIR emission intensity (Fig. 7a), the NIR emission of the $20\text{Yb}/2\text{Er}:\text{NaGdF}_4$ submicrorods doped with $25\% \text{Ca}^{2+}$ and $2\% \text{Ce}^{3+}$ is about 6.4 times higher than that of $20\text{Yb}/2\text{Er}:\text{NaGdF}_4$ submicrocrystals. Notably, the enhanced factor of the sample doped with $25\% \text{Ca}^{2+}$ and $2\% \text{Ce}^{3+}$ is only 2.3, 2.7, respectively. These results suggest that codoping $\text{Ca}^{2+}/\text{Ce}^{3+}$ can greatly enhance the NIR emission intensity. Fig. 7b shows the log-log plots of the NIR emission intensity against laser excitation power of the submicrocrystals doped with no extra ions, $25\% \text{Ca}^{2+}$, $2\% \text{Ce}^{3+}$, and coped with $25\% \text{Ca}^{2+}/2\% \text{Ce}^{3+}$, the experimental data were fitted well with a linear relationship. The quasi-linear power dependence of 1530 nm emission in submicrocrystals doped without Ce^{3+} and quasi-quadratic power dependence in submicrocrystals doped with Ce^{3+} can be observed. The different character of the power-dependent luminescence for the $^4\text{I}_{13/2}$ manifold is possibly due to the competition between UC and linear decay.⁴⁰

To further characterize the NIR emitting properties of the obtained samples, the fluorescence decay curves of the 1530 nm emission for the crystals are shown in Fig. 8. To obtain the decay constants, the luminescence decay curves were fitted by a bi-exponential equation,

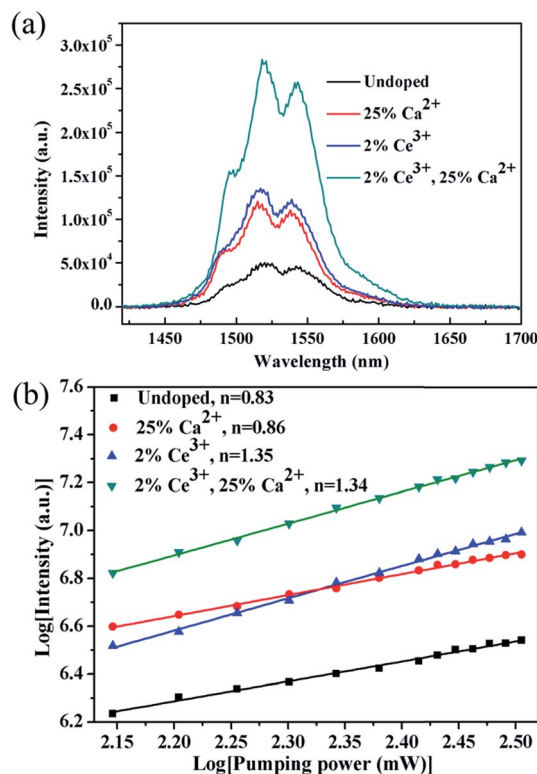


Fig. 7 NIR emission spectra (a) and log-log plots of the NIR emission intensity against laser excitation power (b) of samples single doped with no extra ions, $25\% \text{Ca}^{2+}$, $2\% \text{Ce}^{3+}$, and coped with $25\% \text{Ca}^{2+}/2\% \text{Ce}^{3+}$, the experimental data were fitted well with a linear relationship.



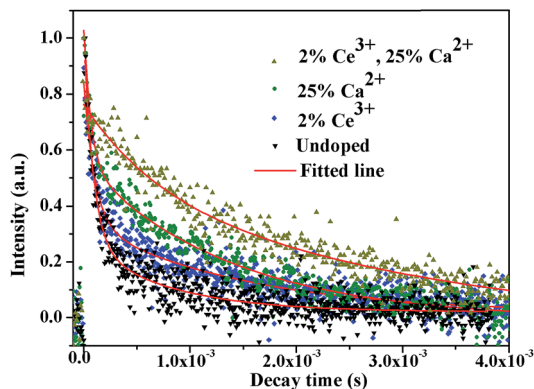


Fig. 8 The decay curves of Er^{3+} 1530 nm emission wavelength upon 980 nm excitation.

$$I(t) = A_1 \times \exp\left(-\frac{t}{\tau_1}\right) + A_2 \times \exp\left(-\frac{t}{\tau_2}\right) \quad (2)$$

where $I(t)$ is the luminescence intensity for the 1530 nm emission, A_1 and A_2 are constants, t is the time, and τ_1 and τ_2 are the corresponding lifetimes for the bi-exponential components. The possible explanations for the double exponential decay of the luminescence could be attributed to two luminescence centers in the host. The ions on the outside of the particles are more susceptible to the defects and high energy vibrational oscillators of ligands or impurities, leading to a larger rate of non-radiative transitions. Therefore, the lifetime of radiative transition of activator ions on the surface (τ_2) is much lower than that in core sites (τ_1). And there is a fact that the decay time can characterize the contributions of both radiative and non-radiative relaxation pathways from a particular excited state. In general, the increased decay time indicates high emission efficiency, which is most likely due to the increased radiative transitions or suppressed non-radiative losses.^{27,41,42} The average fluorescence decay time (τ_{ave}) is obtained using the following expression,⁴³

$$\tau_{\text{ave}} = \frac{A_1 \tau_1^2 + A_2 \tau_2^2}{A_1 \tau_1 + A_2 \tau_2} \quad (3)$$

The estimated decay time increases from $\sim 609.2 \mu\text{s}$ for $\text{NaGdF}_4:20\% \text{ Yb}/2\% \text{ Er}$ to $\sim 1319.6 \mu\text{s}$ for crystals doped with $20\% \text{ Ca}^{2+}$, $\sim 1416.1 \mu\text{s}$ for crystals doped with $2\% \text{ Ce}^{3+}$, and $\sim 2942.5 \mu\text{s}$ for crystals doped with $20\% \text{ Ca}^{2+}/2\% \text{ Ce}^{3+}$, respectively. These results show that $\text{Ca}^{2+}/\text{Ce}^{3+}$ codoping can effectively improve the NIR emission efficiency for $\text{NaGdF}_4:20\% \text{ Yb}/2\% \text{ Er}$ submicrorods.

4. Conclusions

In summary, we have disclosed morphology evolution mechanism and increased visible UC emission intensity of $\text{NaGdF}_4:20\% \text{ Yb}/2\% \text{ Er}$ submicrocrystals induced by Ca^{2+} doping. The influence of Ca^{2+} and Ce^{3+} doping concentration on the NIR emission intensity have been systematically

investigated and the optimized Ca^{2+} and Ce^{3+} doping concentration was 25% and 2%, respectively. The NIR emission intensity was enhanced by ~ 6.4 fold after introducing both of $25\% \text{ Ca}^{2+}$ and $2\% \text{ Ce}^{3+}$. The doping of Ca^{2+} mainly lowers the local crystal field symmetry around the rare earth and improves the morphology of $\text{NaGdF}_4:20\% \text{ Yb}/2\% \text{ Er}$ submicrocrystals. And the doping of Ce^{3+} facilitates the energy transfer between Ce^{3+} and Er^{3+} . Hence, codoping $\text{Ca}^{2+}/\text{Ce}^{3+}$ synergistically enhance the NIR emission intensity. We believe that this novel strategy for simultaneous control of morphology and improving the NIR emission of rare earth doped nano/microcrystals may expand the application in IR-related miniaturization and integration of optoelectronics.

Conflicts of interest

There are no conflicts to declare.

Acknowledgements

The authors would like to acknowledge funding support from the National Natural Science Foundation of China (NSFC) (11574221) and “the Fundamental Research Funds for the Central Universities” (2016SCU11003).

Notes and references

- 1 T. Soukka, K. Kuningas, T. Rantanen, V. Haaslahti and T. Lövgren, *J. Fluoresc.*, 2005, **15**, 513–528.
- 2 F. Wang and X. Liu, *Chem. Soc. Rev.*, 2009, **38**, 976–989.
- 3 X. Xie, N. Gao, R. Deng, Q. Sun, Q.-H. Xu and X. Liu, *J. Am. Chem. Soc.*, 2013, **135**, 12608–12611.
- 4 X. Zhu, Q. Su, W. Feng and F. Li, *Chem. Soc. Rev.*, 2017, **46**, 1025–1039.
- 5 T. Wang, H. Yu, C. K. Siu, J. Qiu, X. Xu and S. F. Yu, *ACS Photonics*, 2017, **4**, 1539–1543.
- 6 R. Dey, A. Pandey and V. K. Rai, *Spectrochim. Acta, Part A*, 2014, **128**, 508–513.
- 7 P. Du and J. S. Yu, *Chem. Eng. J.*, 2017, **327**, 109–119.
- 8 D. Chen, M. Xu and P. Huang, *Sens. Actuators, B*, 2016, **231**, 576–583.
- 9 D. Chen, M. Xu, P. Huang, M. Ma, M. Ding and L. Lei, *J. Mater. Chem. C*, 2017, **5**, 5434–5443.
- 10 K. Korthout, P. F. Smet and D. Poelman, *Appl. Phys. Lett.*, 2009, **94**, 051104.
- 11 J. D. Bradley and M. Pollnau, *Laser Photonics Rev.*, 2011, **5**, 368–403.
- 12 N. Mais, J. P. Reithmaier, A. Forchel, M. Kohls, L. Spanhel and G. Müller, *Appl. Phys. Lett.*, 1999, **75**, 2005–2007.
- 13 J. Wang, J. Hu, D. Tang, X. Liu and Z. Zhen, *J. Mater. Chem.*, 2007, **17**, 1597–1601.
- 14 F. Rivera-López, P. Babu, L. Jyothi, U. R. Rodríguez-Mendoza, I. R. Martín, C. K. Jayasankar and V. Lavín, *Opt. Mater.*, 2012, **34**, 1235–1240.
- 15 Y. P. Fang, A. W. Xu, L. P. You, R. Q. Song, J. C. Yu, H. X. Zhang, Q. Li and H. Q. Liu, *Adv. Funct. Mater.*, 2003, **13**, 955–960.



- 16 G. Gao, C. Zhang, Z. Zhou, X. Zhang, J. Ma, C. Li, W. Jin and D. Cui, *Nanoscale*, 2013, **5**, 351–362.
- 17 A. Shalav, B. S. Richards, T. Trupke, K. W. Krämer and H. U. Güdel, *Appl. Phys. Lett.*, 2005, **86**, 013505.
- 18 D. Chen and P. Huang, *Dalton Trans.*, 2014, **43**, 11299–11304.
- 19 M. Mondal, V. K. Rai and C. Srivastava, *Chem. Eng. J.*, 2017, **327**, 838–848.
- 20 D. Chen, L. Liu, P. Huang, M. Ding, J. Zhong and Z. Ji, *J. Phys. Chem. Lett.*, 2015, **6**, 2833–2840.
- 21 D. Chen and Y. Wang, *Nanoscale*, 2013, **5**, 4621–4637.
- 22 A. K. Singh, S. K. Singh and S. B. Rai, *RSC Adv.*, 2014, **4**, 27039–27061.
- 23 X. Wang, Y. Bu, Y. Xiao, C. Kan, D. Lu and X. Yan, *J. Mater. Chem. C*, 2013, **1**, 3158–3166.
- 24 L. Lei, D. Chen, J. Xu, R. Zhang and Y. Wang, *Chem.-Asian J.*, 2014, **9**, 728–733.
- 25 L. Mukhopadhyay and V. K. Rai, *New J. Chem.*, 2017, **41**, 7650–7661.
- 26 X. Gao, X. Liu, Q. Wen, X. Yang and S. Xiao, *J. Appl. Phys.*, 2014, **116**, 173105.
- 27 X. Zhao and M. C. Tan, *J. Mater. Chem. C*, 2015, **3**, 10207–10214.
- 28 Y. Wang, R. Cai and Z. Liu, *CrystEngComm*, 2011, **13**, 1772–1774.
- 29 X. Liang, X. Wang, J. Zhuang, Q. Peng and Y. Li, *Adv. Funct. Mater.*, 2007, **17**, 2757–2765.
- 30 L. Tian, L. Tan, Q. Sun, S. Xiang, Q. Xiao, J. Tang and G. Zhu, *J. Rare Earths*, 2012, **30**, 1260–1264.
- 31 T. Zhou, X. Jiang, C. Zhong, X. Tang, S. Ren, Y. Zhao, M. Liu, X. Lai, J. Bi and D. Gao, *J. Lumin.*, 2016, **175**, 1–8.
- 32 M. Karbowiak, A. Mech, A. Bednarkiewicz, W. Stręk and L. Kępiński, *J. Phys. Chem. Solids*, 2005, **66**, 1008–1019.
- 33 F. Tao, F. Pan, Z. Wang, W. Cai and L. Yao, *CrystEngComm*, 2010, **12**, 4263–4267.
- 34 Z. Chen, Z. Liu, Y. Liu, K. Zheng and W. Qin, *J. Fluorine Chem.*, 2012, **144**, 157–164.
- 35 D. Chen, Y. Yu, F. Huang, P. Huang, A. Yang and Y. Wang, *J. Am. Chem. Soc.*, 2010, **132**, 9976–9978.
- 36 L. Lei, D. Chen, P. Huang, J. Xu, R. Zhang and Y. Wang, *Nanoscale*, 2013, **5**, 11298–11305.
- 37 X. Peng, J. Wickham and A. Alivisatos, *J. Am. Chem. Soc.*, 1998, **120**, 5343–5344.
- 38 M. Ding, D. Chen, S. Yin, Z. Ji, J. Zhong, Y. Ni, C. Lu and Z. Xu, *Sci. Rep.*, 2015, **5**, 12745.
- 39 Z. Xiong, Y. Yang and Y. Wang, *RSC Adv.*, 2016, **6**, 75664–75668.
- 40 D. Xu, C. Liu, J. Yan, S. Yang and Y. Zhang, *J. Phys. Chem. C*, 2015, **119**, 6852–6860.
- 41 J. W. Stouwdam and F. C. J. M. van Veggel, *Nano Lett.*, 2002, **2**, 733–737.
- 42 J. Wu, S. Shi, X. Wang, J. Li, R. Zong and W. Chen, *J. Mater. Chem. C*, 2014, **2**, 2786–2792.
- 43 T. Fujii, K. Kodaira, O. Kawauchi, N. Tanaka, H. Yamashita and M. Anpo, *J. Phys. Chem. B*, 1997, **101**, 10631–10637.

